Electronic Interface with Vignetting Effect Reduction for a Nikon 6B/6D Autocollimator

Guillermo Bergues, Guillermo Ames, Luis Canali, *Senior Member, IEEE*, Clemar Schurrer
and Ana Georgina Flesia

Abstract—In this paper we present an electronic interface created for the Nikon 6B/6D visual autocollimator which allows for an increase in the final resolution of measurements and a reduction of the vignetting and distortion effects produced by this optical instrument's lenses. The electronic interface consists of a Basler ACE HD camera and its positioning devices, and a computer with a sub-pixel digital image processing package. The latter includes two main procedures: one for scale calibration and the other for determining the position of crosshair lines. Both procedures work at sub-pixel level. The feasibility of the measurement method was verified, and the resolution obtained for the measurement of angular displacements is about 0.019 seconds of arc, ten times better than the one registered by the original visual system. Its overall performance was compared against an electronic level with internationally traceable certification.

Index Terms—visual interface, autocollimator, sub-pixel line detection

I. INTRODUCTION

In manufacturing, automotive, and aerospace industries, there is a need for accurately measuring the geometric parameters of surfaces used in opto mechanical assembly and in the adjustment of optical instruments. Autocollimators are used in such industrial environments for precision alignments of mechanical components, the detection of angular movement and angular monitoring over time, and to ensure compliance with angle specifications and standards, [1]–[3].

Autocollimators operate either by visual detection (by sight) or digital detection using a photodetector, [4]. Visual autocollimators are often used for lining up laser rod ends and checking the face parallelism of optical windows and wedges. Digital autocollimators are used as angle measurement standards for monitoring angular movement over long periods of time, and for checking angular position repeatability in mechanical systems, [5]. A visual autocollimator can measure angles as small as 0.5 seconds of arc, while a digital autocollimator can be up to 100 times more accurate, [6]. Digital autocollimators have a photodetector recording the position of the projected light, thus higher resolution can be achieved increasing the spatial resolution of the detector, or by improving the data processing system, [7], [8]. The detector of the digital autocollimator has been changed many times throughout the past decades, from oscillating slits with photoelectric cells, diodes in a differential circuit to position sensitive detectors (PSD) and charge-coupled device (CCD) arrays, [4]. The first and second detectors are not common nowadays, while the third and fourth are widely used in commercial models. Also, there are some commercial external interfaces that can be acquired to transform visual models into digital ones, such as the Davidson Optronics Digital Autocollimator Upgrade Kit, which allows existing D-652 models to have all the digital functionality of the New Model D-720, Digital Two-Axis Autocollimator. The upgrade kit replaces the autocollimator's eyepiece assembly with a video imager which is controlled by a black box software that allows results to be viewed in real-time, statistically analyzed and stored for later reference, [9].

This paper deals with the design and implementation of an external electronic interface for a Nikon 6B/6D standard visual autocollimator. These high precision autocollimators have a 70mm aperture, which provides bright and clear reflected images and 0.5 seconds of arc resolution within a range of 5 minutes of arc, 1 second of arc resolution within a range of 30 minutes of arc. The interface can be used for monitoring angle deviations in real time. What is more, with slight modifications in the interface's design and in the software that powers it, digital interfaces for other visual autocollimator models can be implemented.

In our previous work, [10], the potential of a low cost interface design was addressed, mounting a simple interface with an off-the-shelf webcam with a CMOS sensor and a wideangle lens. This system allowed us to capture the center of the internal image formed in the autocollimator to later process the information and obtain a measurement. The accuracy and uncertainties measurements were not discussed at the time because the optics of the camera and the positioning device were not reliable enough.

In this paper we extended and improved our previous design [10], [11] by replacing the web-cam with a high resolution Basler Ace camera with CCD sensor, calibrating the camera's position to reduce external errors and by improving the subpixel edge detection algorithm with a preprocessing step to reduce vignetting effects. Our design is similar to the one in Yuan et al. [4], [8]. They discussed an experimental CCD based autocollimator and the final measurement only analyses

G. Bergues, G Ames and L Canali are with CIII – *Centro de Investigación en Informática para la Ingeniería*, UTN-FRC *Universidad Tecnológica Nacional, Facultad Regional Córdoba*, Maestro M. Lopez esq. Cruz Roja Argentina, Ciudad Universitaria, Córdoba, Argentina. gbergues,lames,lcanali@cbasicas.frc.utn.edu.ar

C Schurrer is with CEMETRO – *Centro de Metrología Dimensional*, UTN-FRC *Universidad Tecnológica Nacional, Facultad Regional Córdoba*, Maestro M. Lopez esq. Cruz Roja Argentina, Ciudad Universitaria, Córdoba, Argentina. cschurrer@cbasicas.frc.utn.edu.ar.

A. G. Flesia is with Conicet and FaMAF - *Facultad de Matemática, Astronomía y Física*, UNC - *Universidad Nacional de Córdoba*, Av. Medina Allende, s/n, X5000HUA, Córdoba, Argentina. flesia@mate.uncor.edu

A.G. Flesia is corresponding author.

the zero's long term thermal stability of the system.

In [5], an electronic reference-beam (two mirrors) autocollimator design with nano radian sensitivity was discussed. The design also corrected temperature CCD displacement errors with sub-pixel image processing techniques similar to the ones proposed in [10], [11] and, [12]. The location of curves within an image with sub-pixel resolution is highly interesting in very different fields, such as glass width estimation, [13] and high temperature specimen contour estimation [14], among others.

The interface presented in this paper increases the native resolution of the Nikon 6D autocollimator, without requiring any tampering of the instrument. Our design improves over Yuan et al. [4] in two main points: we deliver a final measurement for the range of the autocollimator, not only the zero value, and our sub-pixel detection algorithm also compensates for vignetting effects.

In Section II, we describe the operational principles of the autocollimator and we describe how we proceeded to perform a measurement with the visual interface. In Section III and IV, we discuss hardware implementation issues and image processing software design. In Section V, four different line detectors were tested under simulation, revealing the power and resilience that the line detector we implemented has to noise and distortion. Section VI shows an experiment made at the CEMETRO laboratory, where interface measurements were compared against measurements from a certified electronic level. In Section VII the results are presented and resolution and uncertainties are discussed as well. The final section shows conclusions and future work.

II. SYSTEM CONFIGURATION

A. Autocollimator

An autocollimator is an optic instrument used for measuring small angular displacements (at the seconds of arc level) (see Fig. 1a). It can perform measurements without making contact with the measured object. To perform a measurement, the autocollimator works together with a reflecting surface E, whose distance to the autocollimator has no influence on the measurement. Its measuring characteristics are expressed in [11] and its calibration ratio is given by (1), where f is the focal distance:

$$\tan(2 \cdot \alpha) = \frac{d}{f}, \tag{1}$$

B. Measurement with Visual Interface

In Fig. 1a, an image of the autocollimator's reticle scale can be seen. In Fig. 1b, the measurement process scheme is presented, as well as the variables pitch (B_y), yaw (B_x) and distance of calibration (Δ_{XY}), which need to be calculated in order to obtain the measurement with the visual interface.

Using Fig. 1b to explain the process, the procedure to perform an automated measurement is:

1) Establish the distance Δ_{XY} between the center of the divisions of the reticle at sub-pixel level. Δ_{XY} uncertainty estimation.
2) Associate a coordinate system (x, y) to the image reticle.
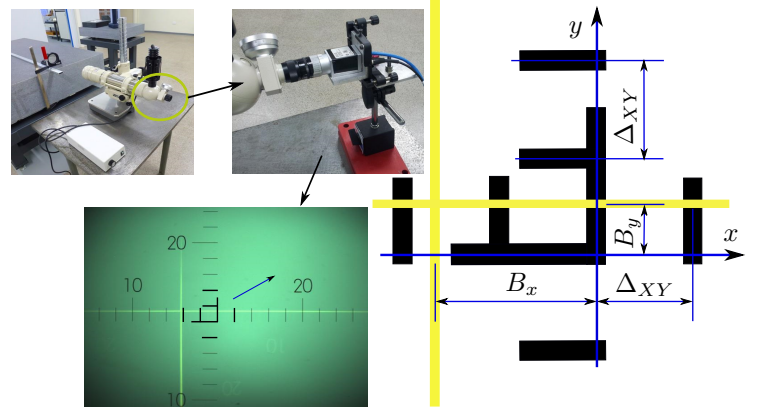
(a) Image of the reticle scale.   (b) Measuring process scheme.

Fig. 1: Correspondence between image and measurement.

3) Identify the crosshair lines at sub-pixel level and measure the distance B_y and B_x between the center of the lines forming the cross with each axis.

For the Nikon 6D autocollimator, the distance between consecutive divisions of the scale represents 60 seconds of arc (1div =1min). Once the value Δ_{XY} of pixels/division is obtained, the observed angle (e.g., pitch) in seconds of arc can be obtained using:

$$\alpha_y = 60 \cdot \frac{B_y}{\Delta_{XY}}, \tag{2}$$

III. DESIGN CONSIDERATIONS

A. Alignment and distortion

Imperfections in positioning and aligning of the camera with the autocollimator's telescope can cause distortions and blur in the CCD-image of the reticle. On the other hand, determining when the camera is in focus is a delicate point [15], [16], since there is a trade-off between picture sharpness and the number of pixels to determine the position of the lines at sub-pixel level. For those reasons an alignment is performed and as a result, the vignetting effect is strongly reduced. The pattern of illumination intensity falloff due to vignetting is such that negligible intensity falloff happens around the image center forming an intensity plateau, whereas significant falloff appears along radial direction from the image center, [17]. This particular pattern is shown in Fig. 2, which is a representation of the real image shown in Fig. 1a.

The alignment strategy is the following: First, we focus and position the camera in such a way that the incoming light to the telescope is centered in the image by moving the camera until the axes of the autocollimator's objective and camera lenses are aligned and the measurement reticle is in focus (see Fig. 2). Next, we align the horizontal cross line with grid camera pixels as shown in Fig. 3, the pixel highs h_1 and h_2, have to be the same $h_1 = h_2$.

B. Capturing the Reticle scale images

The Nikon 6D is a dark field autocollimator: the darker the ambient, the better the precision attained for the operator
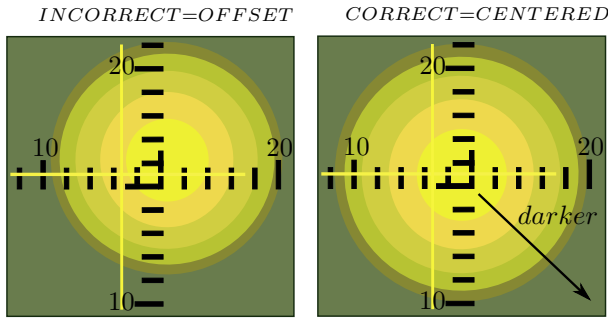
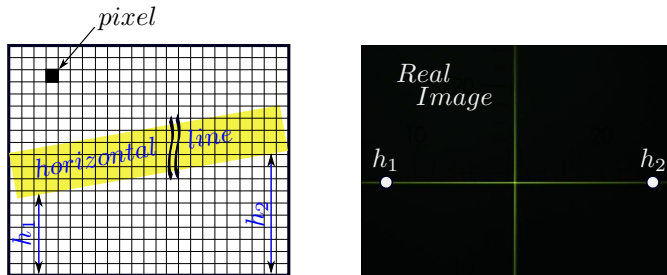Fig. 2: Scheme of how the incoming light has to be seen in the picture.

Fig. 3: Scheme of how to correct the alignment of the lines in respect to the grid camera pixels.

in placing the crosshair lines. However, this situation is not optimal to obtain a good image of the reticle. Scale marks appear distorted and faint in comparison with the crosshair lines, leading to errors in the determination of the Δ_{XY} value. However, the observation of the scale and the crosshair lines can be made separately, with no movements on the positioning system of the camera by simply changing ambient light. Thus, the last step in the system calibration strategy is to take images of the reticle (see Fig.4a) with the ambient lights on in order to maximize the contrast between the clear, bright background and the dark lines of the reticle.

C. Capturing the Crosshair line images

To perform the measurements by determining the displacement of the crosshair lines against the reference scale, the lights in the room were turned off, capturing only images with the crosshair lines (see Fig. 4b) since the background (and the reticle scale) is dark, and the cross itself is bright.
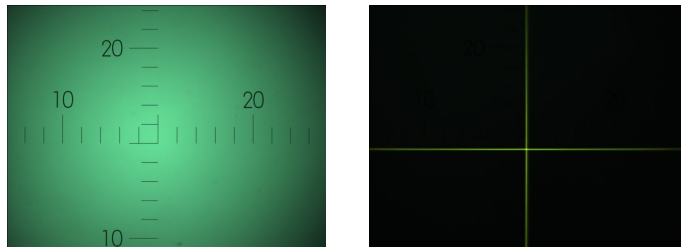
(a) Reticle scale image.   (b) Crosshair line image.

Fig. 4: Image set.

IV. IMAGE PROCESSING

The technique reported in [12] and early versions of our software [10], [11] explain how to find the centroid of each line with the Hough transform and average the centroid locations to calculate the position of each pattern. This method has disadvantages for high sensitivity in low frequency measurements. The CCD pixels were measured to be both nonlinear and noisy at low intensity, but the Hough matrix weights all pixels equally, therefore increased noise in the low intensity pixels and obscures the better sensitivity available from the high intensity pixels.

We developed a new data processing algorithm to reduce these effects. Our algorithm identifies lines by finding local maxima and fitting cross section peaks with a Gaussian function. This algorithm uses robust statistics to fit the data, obtaining good localization even with noise and motion blur (see Fig. 5 for a schematic diagram of the method). Nevertheless, to increase fitting accuracy with small samples, the imagery must be corrected first for the vignetting effect caused by the autocollimator's lenses.
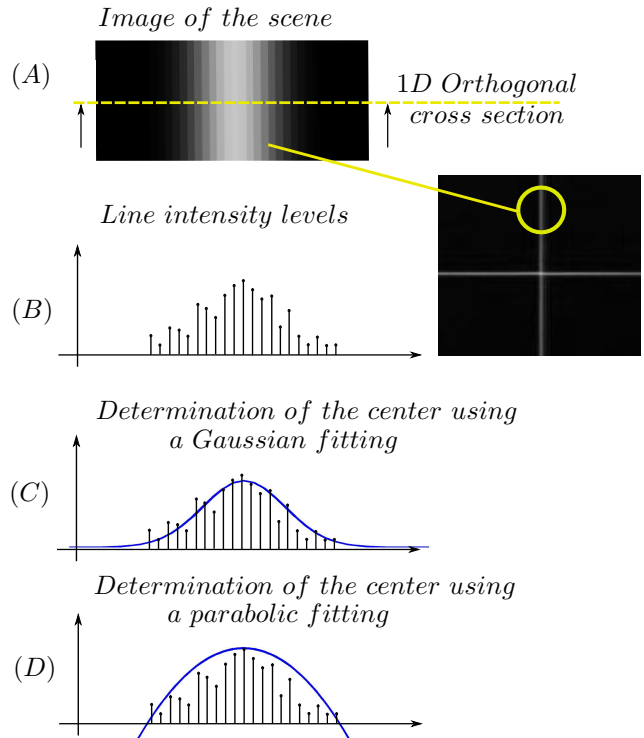

Fig. 5: Schematic diagram of the proposed method for sub-pixel line detection. Cross sections to the edge line detected are shown, with Gaussian and parabolic fitting.

A. Reducing vignetting effects by averaging and filtering

Vignetting effect refers to a position-dependent loss of lighting in the output of an optical system, due mainly to the blocking of a part of the incident ray bundle by the effective size of the aperture stop; resulting in a gradual fading-out of an image at points near its periphery [18]. This effect distorts the imagery taken by the system, introducing a smooth
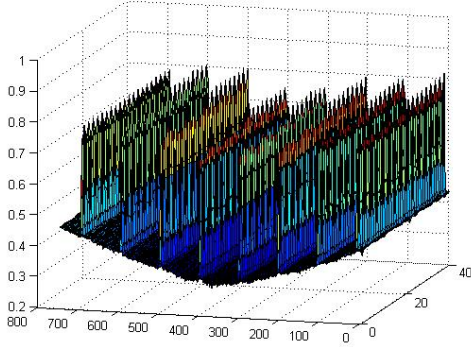
Fig. 6: Vignetting effect over a center piece of the reticle image (3D intensity function).
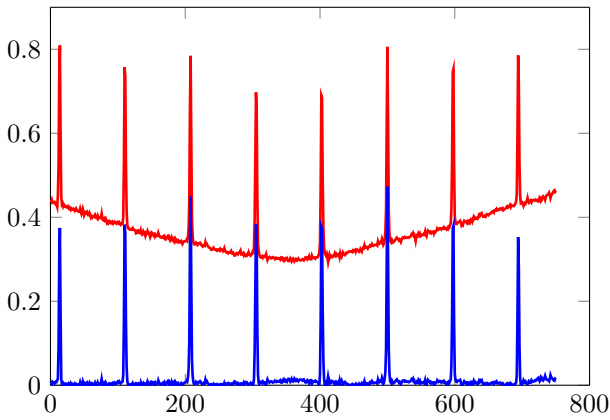

Fig. 7: Cross section of the image in 6: Original curve with Vignetting effect in red; in blue, the same cross section after filtering.

displacement in the centroid of the lines. Fig. 6 shows a 3D section of the reticle showing eight scale marks which appear distorted by this effect: the eight intensity peaks are above a parabolic background which behaves as an offset. Given the smooth character of the background, the Savitzky-Golay filter is an ideal method to reduce the offset. This filter is designed for smoothing images [19], it increases the signal-to-noise ratio without greatly distorting the signal. This is achieved by fitting successive sub-sets of adjacent data points with a second-degree polynomial using the method of linear least squares. Filtering is a step of great importance when using fitting methods, since background noise can greatly reduce the accuracy of sub-pixel location of the edges inside the detected pixel (see Fig 7).

B. Further vignetting correction

After filtering, a residual background could still remain (see Fig. 8). The effect of this offset on the position of the lines in the images can be quantified in the following way: assuming a Gaussian line profile like (4), and with a residual background as $y_B = s_B x + b_B$ after filtering process, the centroid parameter is shifted in first order approximation by:
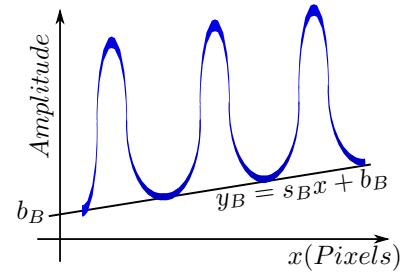

Fig. 8: Residual background $y_B = s_B x + b_B$ affecting the position and height of each Gaussian function.

$$\Delta_B = s_B * \sigma^2 \qquad (3)$$

where s_B is the slope of the residual background and σ the width of Gaussian function. The Δ_B value will be very important for the uncertainty discussion in section VII-C.

C. Subpixel line detection

Cross sections of smooth intensity lines can be modeled with a bell or parabola shape, as shown in Fig. 5. For these models, the determination of the line center at sub-pixel level is given by a parameter when a Gaussian function is considered, or combination of parameters in the case of the parabola shape.

Our algorithm for sub-pixel straight lines detection has three steps: the sharpening of the image using a version of the Savitzky-Golay filter for smoothing and differentiation; pixel level line center detection; and finally, sub-pixel center location determination obtained by fitting a Gaussian function to cross sections (orthogonal sections) passing each detected line center at the pixel level.

The center of the line at pixel level is detected by analyzing the intensity matrix in search of maximum intensity values. Around each of the pixels, a linear neighborhood L (cross section) orthogonal to each detected line position is extracted (see Fig. 5), and the location of the maximum of the fitted cross section of the Gaussian function S_V is obtained, see (4). This function has three parameters: the centroid b (the center of the line), the pair a, and σ which give the bell's height and width respectively.

$$S_V = a * e^{-(x-b)^2/\sigma^2} \quad x \in L \qquad (4)$$

In the literature, second order polynomials

$$S_V = A_1 x^2 + A_2 x + A_3 \quad x \in L \qquad (5)$$

are also used for fitting when only few samples are available in the neighborhood, as the result of the camera's coarse resolution, [20]. What is more, blurred edges have also been sharpened by this sub-pixel methods, fitting second order polynomials [14].

In our case, second order polynomials are very sensitive to the size of the neighborhood, as well as to the symmetry of the neighborhood around the center of the line at pixel level. In Fig. 9, we show a discrete edge curve, defined

in a neighborhood of $N = 44$ pixels around a detected line center, with a Gaussian and quadratic fitting asymmetric neighborhoods. For quadratic fitting, we observe that the small centered neighborhood gives a good estimate of the sub-pixel position of the edge point, but the asymmetric neighborhood provides a biased estimate of the subpixel location. On the other hand, the Gaussian fitting proved to be insensitive to the size and symmetry of the neighborhood.
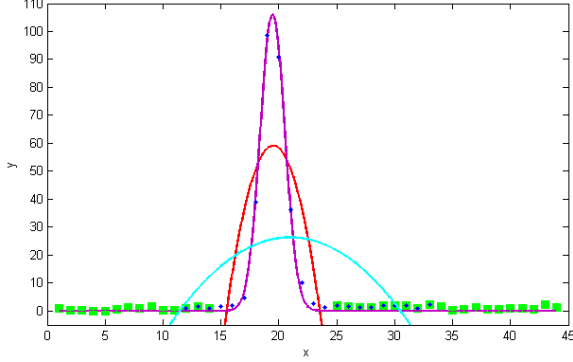

Fig. 9: Second order polynomial approximations to the cross section curve. In red, approximation made using a small symmetric L neighborhood (discarded values in green) centered on the coarse edge pixel. In cyan, approximation made using a biased neighborhood L (marked in blue). Gaussian fitting in purple was computed with all data.

V. Simulation

To carry out the analysis of the methods described above, the line model that is considered is defined by a sub-pixel level centroid Gaussian profile (c), see Fig. 5B. 100 images were created using a software. Each image describes a parallelly displaced line with a centesimal step (chosen sub-pixel value). In this way, the real lines of both the cross and the scale of a Nikon 6B/6D autocollimator are represented [12]. Using this simulated data -since we worked in a known environment-, it was possible to understand, analyze and depure the behaviour of each simulated detector in order to establish the optimum detection algorithm for the designed interface.

The equation that was used to generate the Guassian line in an image I formed by a matrix (N_x, N_y), was the following:

$$I(i,j) = round(A.e^{\frac{-(j_0-j)^2}{2.\Delta^2}}), \; j_0 = \frac{N_y}{2} \in N \quad (6)$$

The values of c to be estimated are j_0+k with $k = \frac{1}{100}$. The $round$ function is the round to the nearest integer function. The width of the line given by Δ allows us to build a line according to the number of pixels that the line in the captured images occupies. Where:

$$0 \leq I(i,j) \leq 255 \; e \; I(i,j) \in N \quad (7)$$

A. Hough Detector

The Hough transform allows for the transformation of the binary border image's discreet space, which is made up of pixels, into the parametric space (see 10) which is a function of θ y ρ, variables which define a straigth line:

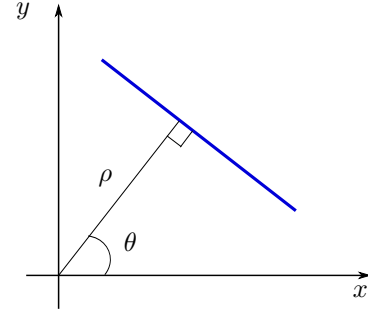$$\rho = x \cdot cos(\theta) + y \cdot sen(\theta), \quad (8)$$

Fig. 10: Parametric space of a straight line.

In the usual transform [21], [22], the data contained in the gray levels is almost entirely lost when the thresholding deriving in a binary image is performed. Pre-processes of thresholding and edge detection can both be excluded if a new parametric space is created. This parametric space must include all the information provided by each gray level [23]. The algorithm designed in [23] detects bands with only one gray value. This approximation is inadequate for metrologic measures with autocollimators in which the position of a line has to be obtained at sub-pixel precision (what is important is not the band, but its central position).

1) Gray Hough parameter counting space: Based on Eq. (8), with a space of image given by (x, y, G), in which G is the gray level corresponding to each point (x, y) of the image, a new parametric space is formed:

$$\rho(G) = x \cdot cos(\theta(G)) + y \cdot sen(\theta(G)), \quad (9)$$

This parametric space defines a mapping space f : $(x, y, G) \rightarrow H(\rho, \theta, G)$ which builds H_i accumulators that correspond to each gray level. All the accumulators derive in a density function whose maximum values correspond to the center of each line. $2^{n^{\circ}bits}$ accumulators -unified in a 3D matrix- are created, being n the quantization bits number of the camera.
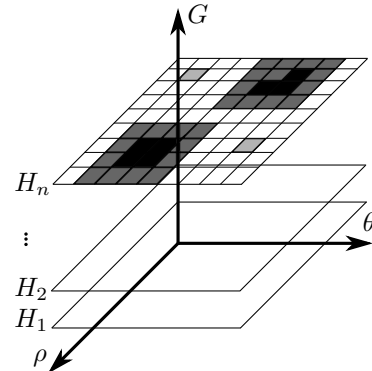

Fig. 11: Gray Hough parameter counting space.

In Fig. 11, as an example, the local maximum values of

the H_n accumulator are shown. The color black responds to the region most likely to encounter a straight line for the gray level n. The following algorithm summarizes the procedure:

1) Initialize each accumulator $H(\rho, \theta, G)$ a 0
2) For each pixel (x, y, G) y $\theta_j = 0° \to 179°$
3) Calculate $\rho_j(G_i) = x_i \cdot cos(\theta_j(G_i)) + y_i \cdot sen(\theta_j(G_i))$
4) $H(\rho_j, \theta_j, G_i) = H(\rho_j, \theta_j, G_i) + 1$
5) Creation of the final matrix $H_T = H_1 + ... + H_n$
6) Obtention of the points with the highest degree of probability in the parametric plane.
7) Map these points onto the image plane and obtain the density function center that is defined by them.

B. Probabilistic detector

According to the line profile sampled (ver Fig. 5B), another detector was created in accordance with the probabilistic weighted mean. Being each profile value a sample x and its amplitude, the weight (probability distribution) $P_{(x)}$, we can express the following discreet variable , each orthogonal cut being cv; and N the number of points per cut:

$$< x >= \sum_{i=1}^{N} x_i \cdot P_{(x_i)}, \quad x = (1, ..., N)', \qquad (10)$$

$$P = (P_{(x_1)}, ..., P_{(x_N)})', \quad P_{x_i} = \frac{cv}{\sum_{i=1}^{N} cv_i}, \qquad (11)$$

C. Maximum Value Detector

An algorithm that finds the maximum of the vertical cuts shown in (ver Fig. 5B) is defined through this algorithm:

1) Given an imageDada una imagen $I(M, N)$
2) Generate N samplings cv of the line..
3) Obtain the maximum values of M_{cv_i} cutting functions.
4) Detection of the center $c_i = (\sum_{i=1}^{N} M_{cv_i})/N$

D. Weighted Least Squares Detector

Using the whole of the image intensity matrix, 3 vectors are formed which will determine the regression line $y = a \cdot x + b$ that intercepts the center of the sought line (ver Fig. 12). The b parameter gives the center of each line. The summed square of residuals s (Eq. 12) is minimized, and the result of this process gives the parameter values of the regression lines a and b.

$$s = \sum_{i=1}^{N} W_i \cdot (y_i - (a \cdot x_i + b))^2, \qquad (12)$$

where each weight W_i, is given by:

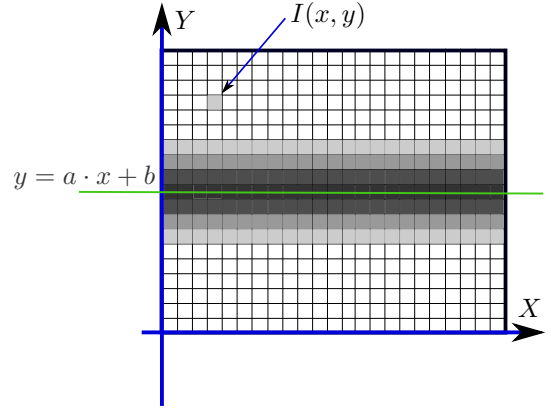$$W_i = \frac{I(x, y)}{\sum_{i=1}^{N} I(x, y)}, \qquad (13)$$

Fig. 12: Regression line $y = a \cdot x + b$ that intercepts the center of the line formed by different gray levels. Each pixel has an intensity value $I(x, y)$ which is function of the spatial coordinates (x, y).
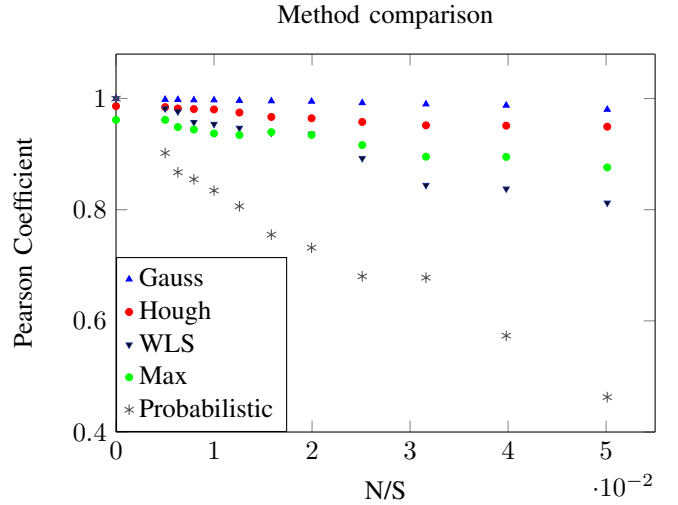

Fig. 13: Detection Characteristics according to the noise level N/S present for all detectors.

E. Simulation Results with and without Noise

The images captured have a signal-noise relation S/N of $13dB$. After applying the Satvizky-Golay filter, a $(S/N = 23dB)$ is obtained. For each noise level in between these extremes, 100 images with sub-pixel step $\frac{1}{100}$ were created. Taking into acount the subpixel centroid values c' estimated for each detector as a linear function of the simulated centroids c, the Pearson correlation coefficient r [24] is used as a quality estimation measurement. In Fig 18, the results of r for the different detectors and noise levels (N/S) are shown.

The probabilistic detector (r_P) and the maximum value detector (r_M) are very influenced by noise level. The Least squares detector (r_R) is not so influenced by noise level as the others mentioned before, although it does not surpass the Gaussian nor the Hough detector in the detections we are interested in (without noise and with $S/N = 23dB$). The Hough detector (r_H) obtains good values for the relevant points. However, the Gaussian detector (r_G) is the one that is most successful in obtaining the center of the straight line

at sub-pixel level. On the other hand, the r_H values show that the Hough Transform is a reliable alternative method (values of $r > 0.95$ are acceptable).

F. Results of Simulation with Bent Line

The two most accurate detectors were chosen. Their behaviour was studied as the simulated line was being bent. The angles that were studied are the ones generated in the spatial resolution's original image $(1234, 1624)$ (see Fig. 14). In Fig. 15, it is possible to observe how the Gaussian detector remains unaffected by the bending, while the Hough detector is deteriorated as the bending increases. On the other hand, a maximum value for the bending $\alpha = 0.07°$ can be observed in the Hough detector. These data is used in the initial calibration when the Hough sub-pixel detector is utilized.
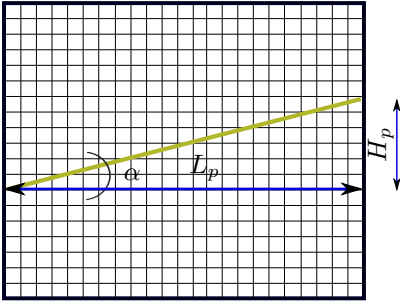

Fig. 14: Bent line parameters. If we vary the height H_p in pixels and maintain $L_p = 1624$ steady, we obtain different values for α.

According to the results expressed in this simulation, a study on the real images captured was carried out in order to obtain the final performance of the Gaussian algorithm selected (it was also compared to the Hough algorithm in this final step). This final comparison can be looked at in Fig. 18.
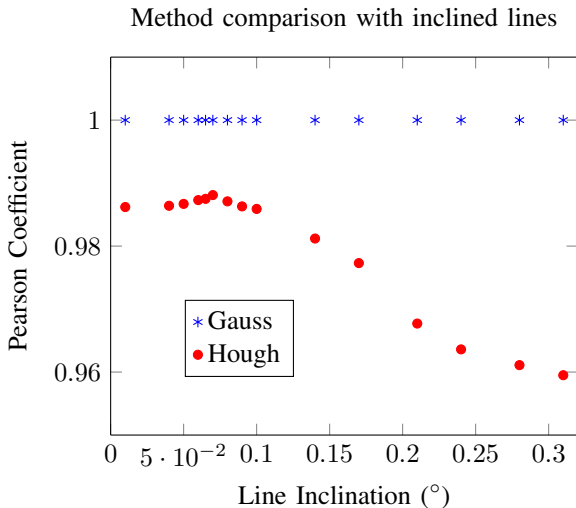

Fig. 15: Detection characteristics according to line bending for Hough and Gaussian detector.

VI. MEASURING EXPERIMENT

A. Controlled experiment

To validate the feasibility of the measurement method with the visual interface, a controlled experiment was designed: different angles were generated using a micrometric screw and measured simultaneously using the system under test (autocollimator + camera + software) and an electronic level. The Mahr electronic level was used as reference. The electronic level is a Mahr Federal EMD-832P-48-W2; Serial Number 2095-06293. This instrument is available at the Laboratory where the experiment is performed (CEMETRO, UTN Córdoba) and it is readily traceable to internationally accepted standards. The electronic level resolution is 0.1 seconds of arc and the accuracy is within 2%.

The digital interface was calibrated with a total of 200 images of the reticle, filtered and corrected. The mirror E and the electronic level N were placed on a bar that can rotate around an axis. Bar rotation was regulated by means of a micrometric screw T placed on one of its ends (see Fig. 16). The working assumption is that the electronic level N, for the k-th position of screw T generates a reference measurement of a pitch angle, so the results of the experiment were ordered pairs (X_k, α_k), being X_k the electronic level reading and α_k the digital reading of the autocollimator measurement.

Fig. 16: Experience with electronic level and autocollimator.

B. Establish the distance Δ_{XY}

Using the algorithm shown in Fig. 17A and the above controlled experience for capturing the images, the reticle must be calibrated, obtaining the value Δ_{XY}.

In separate procedures, we located the eight central scale marks in vertical and horizontal direction, obtained their sub-pixel position with Gaussian fitting, and estimated the autocollimator scale pitch using a simple regression model given by:

$$p_k = \Delta_{XY} * k + \epsilon, \quad k : 1, \dots, 8, \quad \epsilon \sim N(0, \sigma). \quad (14)$$

Estimated sub-pixel values for the autocollimator scale pitch on each axis were coincident within the 95% confidence interval. Therefore, a mean value for scale calibration was set as:

$$\Delta_{XY} = (97.31 \pm 0.02) \text{pixels/division (95\% confidence)}. \quad (15)$$

This allowed us to conclude that scales are linear within an uncertainty margin of 0.02 pixels/div for both axes. In [10], we discuss the benefits of modeling the eight scale marks with
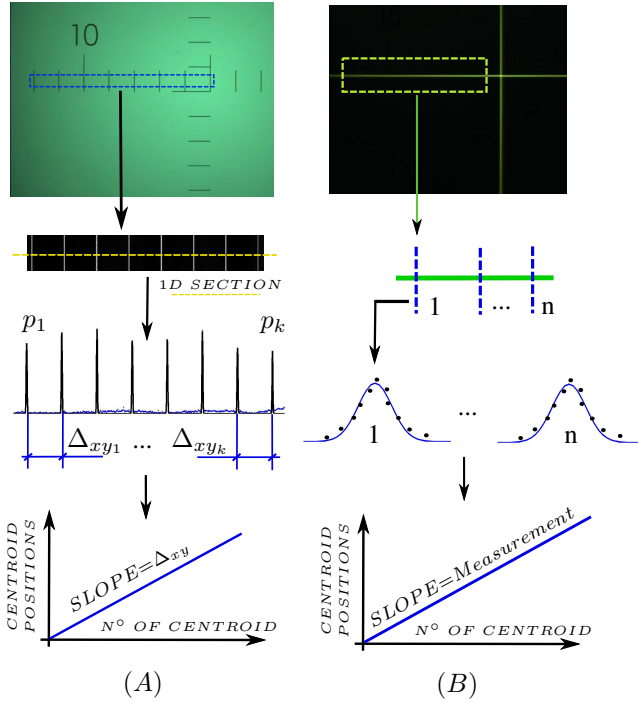
Fig. 17: Flowcharts of detection.

a Gaussian mixture with fixed step Δ_{XY} and we compare it with a linear regression model to estimate such step. The model suggested here has more degrees of freedom, since all Gaussian fits are computed independently. The CMOS camera used in [10] needs a stringiest model to cope with the reduced resolution and smaller signal to noise ratio (SNR).

C. Subpixel crosshair lines' position estimation

Applying the algorithm schematized in Fig. 17B, the position of the one dimensional straight lines were estimated with the centroid B_k of a Gaussian fit to a cross section of the line detected at pixel level, as it was carried out with the scale.

The value α_k was the relative position with respect to centroid B_1, corresponding to the reference value (first measurement) of the visual interface and the electronic level. It was converted to seconds of arc using:

$$\alpha_k = \frac{(B_k - (B_1)) * 60}{\Delta_{XY}} = \frac{(B_k - (B_1)) * 60}{97.31}. \quad (16)$$

VII. RESULTS AND DISCUSSION

A. Resolution discussion

Given the r_G values in function of N/S, a regression curve is determined by:

$$r_G = 1 + 0.0658 \cdot X \cdot ln(X), \quad X = N/S \quad (17)$$

Each r_G, in accordance with this regression line, a quadratic mean s given by:

$$s = L \cdot \frac{1}{\sqrt{12}} \sqrt{\frac{N}{N-2}} \sqrt{\frac{1}{r_G^2} - 1} \quad (18)$$

L is the simmulation interval's width; and N is the number of points used. The maximum intensity is 2^n per pixel; therefore, the best N/S relation that could be expected is $1 pixel/2^n pixels$. In this way, it is possible to calculate which is the smallest N/S for the different numbers of bits. The Rayleigh criterion (in optics) says that two lines can be distinguished if they are separated at least by the sum of its half-widths. Using this (universally accepted) criterion, and extending it to our case, we can define the expected minimum resolution as $R_n = s$. This quantity includes the properties of the algorithm, the spatial resolution of the camera, the relative width of the line, and the intensity resolution of the camera; that is to say, all the properties of the image and their processing. For this instance: $8 bits$ camera, the $R_n = 0.0195$. The other defects: autocollimator's optic, camera's optic, its possible misalignments, unlinearity of the CCD in X, Y; are part of the uncertainty measure (explained in section VII-C).

B. Comparison of measurements performed with the modified autocollimator and the electronic level

The data (X_k, α_k) for $k = 1...25$ were fitted with a linear regression model:

$$\alpha_k = a * X_k + b + \epsilon, \quad \epsilon \sim N(0, \sigma) \quad (19)$$

The slope was $a = 1.0232 \pm 0.0004$ (95% confidence) and the intercept was $b = 0.81 \pm 0.02$ seconds of arc (95% confidence). The difference between (a) and unity is near 2%. This value is very close to the electronic level accuracy.

The error in the fitting caused by the calibration of the Electronic Level was disregarded because this research is focused on the new instrument's resolution. The discrepancies are defined by (see Fig. 18):

$$D_k = \alpha_k - (a * X_k + b) \quad (20)$$

The mean square value (D_{rms}) of discrepancies calculated in this controlled experiment was:

$$D_{rms} = \sqrt{\frac{\sum_k D_k^2}{25}} = 0.04" \quad (21)$$

This quantity is an estimation of the instrument's accuracy (autocollimator plus camera) as it is defined in VIM-2008 (item 2.3 Note 3). The previous definition of resolution (R_n) satisfies $Rn < D_{rms}$ and can be used to estimate the resolution gain G of the vision system with respect to that of the instrument $(R = 0, 5")$:

$$G = \frac{R}{R_n} = \frac{0.5}{0.0195} = 25.64 \sim 25 \quad (22)$$

The results show an increase in the instrument's measurement resolution when the operator is replaced by an automated procedure using this electronic interface.

C. Uncertainty Discussion

According to JCGM (Joint Committee for Guides in Metrology) [25], the combined standard uncertainty $u_c^2(y)$ is given by:
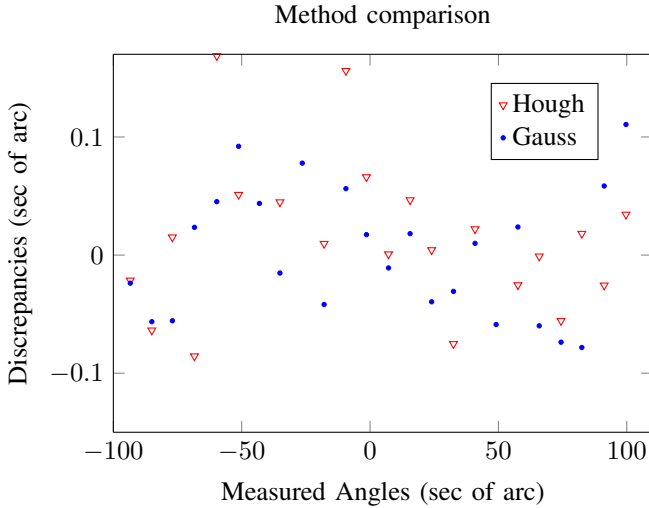
Method comparison

Fig. 18: Detection characteristics on the real image for all Gaussian and Hough detectors according to the noise level N/S present. The Gaussian detector shows less overall discrepancy, as it is maintained within a range of $\pm 0,1$ seconds of arc. The Hough detector's range, however, is within $\pm 0,15$.

$$u_c^2(y) = \sum_{i=1}^{N} \left(\frac{\partial f}{\partial x_i} \right)^2 u^2(x_i) \qquad (23)$$

Applied to our case, using (1):

$$u_c^2(\alpha) = \left(\frac{60}{\Delta_{XY}} \right)^2 u^2(B_y) + \left(\frac{60.B_y}{\Delta_{XY}^2} \right)^2 u^2(\Delta_{XY}) \quad (24)$$

Where the value of $u^2(\Delta_{XY})$ is given by:

$$u(\Delta_{XY}) = \sqrt{(u_{noise}^2 + u_{BIAS}^2)} \qquad (25)$$

$u_{noise} = 0.01$ is the uncertainty associated with random noise obtained directly from the regression model applied to obtain (15). Using equation (3), u_{BIAS} could be estimated as:

$$u_{BIAS} = \frac{2 * \Delta_B}{97.31 * 7} = 0.001 \qquad (26)$$

Even if in our case $u_{BIAS} << u_{noise}$, care must be taken in the filtering process. On the other hand, the uncertainty $u(B_y)$ has a weak effect due to vignetting because when the B_y measurements were performed, the background was dark. For this reason we can roughly approximate $u(B_y) = u_{noise}$, which gives an uncertainty $u_c(\alpha) = 0.015$ seconds. Comparing this result with (21), we conclude that $u_c(\alpha)$ is underestimated because uncertainties related to ambient conditions, autocollimator and CCD nonlinearities, etc. which were not included. A more detailed analysis of this item is out the scope of the present work and will be included in another communication.

VIII. CONCLUSIONS AND FUTURE WORK

In this paper, the main characteristics of an electronic interface are described. The interface comprises a CCD camera and an image processing package custom built around Matlab environment. The image package includes two main procedures, one for reticle scale calibration and another to determine the position of the crosshair lines. The main method used for image processing was chosen from a detailed simulation.

The measurements were performed using the two set of images obtained independently from each other. The reticle scale images were used to obtain the distance between two consecutive divisions of the scale and the crosshair lines were used in angles measurement. The procedure to obtain the reticle scale value Δ_{XY} is carried out just once, since it depends solely on camera resolution and not on measured values.

The interface was set up to improve the resolution of measurements performed with a standard Nikon 6B/6D dark field autocollimator. The results indicate that an increment in resolution is feasible. The key for angle calculation is the use of filtered and corrected image sections that were modeled with Gaussian functions. Centroids of these functions allow for the determination of the position of each line of the scale with sub-pixel resolution.

The choice of this algorithm was carried out through a process of rigorous analysis using simulation. This simulation included many algorithms that were tested under different noise levels and with bent lines, thus allowing for a definition of the optimal.

In order to calibrate the whole range of the autocollimator (30 minutes of arc) it will be necessary to obtain a more accurate reference for the angle values and an improved experimental setup to generate angles covering the whole range of the autocollimator. On the other hand, to obtain reliable measurements at sub-pixel level, it is necessary to give all the contributions to the uncertainty of the measured angles with a detailed analysis of each one according to ISO-GUM. This will be done in a future publication.

REFERENCES

[1] K. Li, C. Kuang, and X. Liu, "Small angular displacement measurement based on an autocollimator and a common-path compensation principle," *Review of Scientific Instruments*, vol. 84, no. 1, 2013.

[2] A. Kirsanov, T. Barmashova, V. Zelenogorskii, and A. Potemkin, "Computer-aided two-coordinate autocollimator for measuring small angular deviations," *Instruments and Experimental Techniques*, vol. 52, no. 1, pp. 141–143, 2009.

[3] R. Soufli, M. Fernández-Perea, S. L. Baker, J. C. Robinson, E. M. Gullikson, P. Heimann, V. V. Yashchuk, W. R. McKinney, W. F. Schlotter, and M. Rowen, "Development and calibration of mirrors and gratings for the soft x-ray materials science beamline at the linac coherent light source free-electron laser," *Appl. Opt.*, vol. 51, no. 12, pp. 2118–2128, Apr 2012.

[4] J. Yuan and X. Long, "Ccd-area-based autocollimator for precision small-angle measurement," *Review of Scientific Instruments*, vol. 74, no. 3, pp. 1362–1365, 2003.

[5] T. Arp, C. Hagedorn, S. Schlamminger, and J. Gundlach, "A reference-beam autocollimator with nanoradian sensitivity from mhz to khz and dynamic range of 107," *Review of Scientific Instruments*, vol. 84, no. 9, pp. 095 007–095 007–7, Sep 2013.

[6] S. Alcock, K. Sawhney, S. Scott, U. Pedersen, R. Walton, F. Siewert, T. Zeschke, F. Senf, T. Noll, and H. Lammert, "The diamond-nom: A non-contact profiler capable of characterizing optical figure error with sub-nanometre repeatability," *Nuclear Instruments and Methods in Physics Research Section A: Accelerators, Spectrometers, Detectors and Associated Equipment*, vol. 616, no. 23, pp. 224 – 228, 2010.

[7] J.-b. Tan, L. Ao, J.-w. Cui, and W.-j. Kang, "Further improvement of edge location accuracy of charge-coupled-device laser autocollimators using orthogonal fourier-mellin moments," *Optical Engineering*, vol. 46, no. 5, pp. 057 007–057 007–12, 2007.

[8] J. Yuan, X. Long, and K. Yang, "Temperature-controlled autocollimator with ultrahigh angular measuring precision," *Review of Scientific Instruments*, vol. 76, no. 12, pp. –, 2005.

[9] Davidson-Optronics. [Online]. Available: http://davidsonoptronics.com/products/autocollimators/d652/

[10] C. Schurrer, A. Flesia, G. Bergues, G. Ames, and L. Canali, "Interfaz visual para un autocolimador nikon 6d mediante procesamiento de imágenes con precisin sub-píxel: un caso de estudio," *Revista Iberoamericana de Automática e Informática Industrial - RIAI*, vol. 11, no. 3, pp. 327–336, 2014.

[11] G. Bergues, G. Ames, L. Canali, C. Schurrer, and A. Flesia, "External visual interface for a nikon 6d autocollimator," in *Instrumentation and Measurement Technology Conference (I2MTC) Proceedings, 2014 IEEE International*, May 2014, pp. 35–39.

[12] A. Flesia, G. Ames, G. Bergues, L. Canali, and C. Schurrer, "Subpixel straight lines detection for measuring through machine vision," in *Instrumentation and Measurement Technology Conference (I2MTC) Proceedings, 2014 IEEE International*, May 2014, pp. 402–406.

[13] J. Park, J. Lee, M. Lee, and E. Lee, "A glass thickness measuring system using the machine vision method," *International Journal of Precision Engineering and Manufacturing*, vol. 12, no. 5, pp. 769–774, 2011.

[14] A. Fabijaska and D. Sankowski, "Computer vision system for high temperature measurements of surface properties," *Machine Vision and Applications*, vol. 20, no. 6, pp. 411–421, 2009.

[15] N. T. Goldsmith, "Deep focus; a digital image processing technique to produce improved focal depth in light microscopy," *Image Analysis and Stereology*, vol. 19, no. 3, pp. 163–167, 2011.

[16] D. Vollath, "The influence of the scene parameters and of noise on the behaviour of automatic focusing algorithms," *Journal of Microscopy*, vol. 151, no. 2, pp. 133–146, 1988.

[17] Y. Wonpil, "Practical anti-vignetting methods for digital cameras," *Consumer Electronics, IEEE Transactions on*, vol. 50, no. 4, pp. 975–983, Nov 2004.

[18] E. Hecht, *Optics (4th Edition)*, 4th ed. Addison Wesley, Aug. 2001.

[19] R. Schafer, "What is a savitzky-golay filter? [lecture notes]," *Signal Processing Magazine, IEEE*, vol. 28, no. 4, pp. 111–117, July 2011.

[20] P. Zhao, W. Zhao, Z. Duan, and W. Zhao, "Subpixel-precise edge extraction algorithm based on facet model," in *Computational and Information Sciences (ICCIS), 2012 Fourth International Conference on*, Aug 2012, pp. 86–89.

[21] W. C. K. N.Aggarwal, "Line detection in images through regularized hough transform," *Transactions on Image Processing*, vol. 15, no. 3, pp. 582–591, 2006.

[22] P. H. R. O. Duda, *ACM*.

[23] R.-C. Lo and W.-H. Tsai, "Gray-scale hough transform for thick line detection in gray-scale images." *Pattern Recognition*, vol. 28, no. 5, pp. 647–661, 1995.

[24] E. B. Niven and C. V. Deutsch, "Calculating a robust correlation coefficient and quantifying its uncertainty," *Computers and Geosciences*, vol. 40, no. 0, pp. 1–9, 2012.

[25] J. C. for Guides in Metrology, "Jcgm 100: Evaluation of measurement data - guide to the expression of uncertainty in measurement," JCGM, Tech. Rep., 2008.